

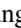



## Spallation and fragmentation cross sections for 168 MeV/nucleon $^{136}\text{Xe}$ ions on proton, deuteron, and carbon targets

X. H. Sun <sup>1,2,\*</sup> H. Wang <sup>2,†</sup> H. Otsu,<sup>2</sup> H. Sakurai,<sup>2</sup> D. S. Ahn,<sup>2</sup> M. Aikawa,<sup>3</sup> N. Fukuda,<sup>2</sup> T. Isobe,<sup>2</sup> S. Kawakami,<sup>4</sup> S. Koyama,<sup>5</sup> T. Kubo,<sup>2</sup> S. Kubono,<sup>2</sup> G. Lorusso,<sup>2</sup> Y. Maeda,<sup>4</sup> A. Makinaga,<sup>6,7,8</sup> S. Momiyama,<sup>5</sup> K. Nakano,<sup>9</sup> S. Nakayama,<sup>10</sup> M. Niikura,<sup>5</sup> Y. Shiga,<sup>11,2</sup> P.-A. Söderström,<sup>2</sup> H. Suzuki,<sup>2</sup> H. Takeda,<sup>2</sup> S. Takeuchi,<sup>2</sup> R. Taniuchi,<sup>5,2</sup> Ya. Watanabe,<sup>2</sup> Yu. Watanabe,<sup>9</sup> H. Yamasaki,<sup>5,‡</sup> X. F. Yang <sup>1</sup> Y. L. Ye <sup>1</sup> and K. Yoshida<sup>2</sup>

<sup>1</sup>*School of Physics and State Key Laboratory of Nuclear Physics and Technology, Peking University, Beijing 100871, China*

<sup>2</sup>*RIKEN Nishina Center, 2-1 Hirosawa, Wako, Saitama 351-0198, Japan*

<sup>3</sup>*Faculty of Science, Hokkaido University, Sapporo 060-0810, Japan*

<sup>4</sup>*Faculty of Engineering, University of Miyazaki, Miyazaki 889-2192, Japan*

<sup>5</sup>*Department of Physics, Graduate School of Science, University of Tokyo, 7-3-1 Hongo, Bunkyo, Tokyo 113-0033, Japan*

<sup>6</sup>*Graduate School of Medicine, Hokkaido University, North-14, West-5, Kita-ku, Sapporo 060-8648, Japan*

<sup>7</sup>*JEIn Institute for Fundamental Science, NPO Einstein, Kyoto 606-8317, Japan*

<sup>8</sup>*Faculty of Fukuoka Medical Technology, Teikyo University, 6-22 Misakimachi, Omuta-shi, Fukuoka 836-8505, Japan*

<sup>9</sup>*Department of Advanced Energy Engineering Science, Kyushu University, Kasuga, Fukuoka 816-8580, Japan*

<sup>10</sup>*Nuclear Data Center, Japan Atomic Energy Agency, Ibaraki 319-1195, Japan*

<sup>11</sup>*Department of Physics, Rikkyo University, 3-34-1 Nishi-Ikebukuro, Toshima, Tokyo 171-8501, Japan*



(Received 6 July 2019; revised manuscript received 13 March 2020; accepted 2 June 2020; published 25 June 2020)

The spallation and fragmentation reactions of  $^{136}\text{Xe}$  induced by proton, deuteron, and carbon targets at 168 MeV/nucleon were studied at RIKEN Radioactive Isotope Beam Factory via the inverse kinematics technique. A wide range of isotopic distributions of the reaction cross sections has been obtained and systematically analyzed by using the Particle and Heavy Ion Transport code System (PHITS) including dynamical and intranuclear cascade processes plus evaporation process, the semi-empirical parametrization for residue cross sections in spallation reactions (SPACS) and empirical parametrization of fragmentation cross sections (EPAX), and the deuteron-induced reaction analysis code system (DEURACS) incorporating the deuteron breakup effect. The carbon target has exhibited strong potential to produce light-mass isotopes far away from the projectile, in comparison to proton and deuteron targets. This may be attributed to the possible higher excitation energies of the prefragment induced by heavier target. It is demonstrated that the deuteron target has advantages to produce isotopic chains very close to the projectile and also the neutron-rich nuclei in other isotopic chains far away from the projectile, due basically to its structure property and the effect of the breakup neutron in the peripheral collision processes. The proton target has the advantage of being able to produce isotopes produced via charge-pickup reactions in comparison to other targets. The prediction powers of various calculation codes are examined with respect to the experimental isotopic distributions. The target and energy dependences of the produced mass distributions are also discussed.

DOI: [10.1103/PhysRevC.101.064623](https://doi.org/10.1103/PhysRevC.101.064623)

### I. INTRODUCTION

Spallation and/or fragmentation reactions have long been known to be crucial in both fundamental research and application fields. These reactions are promising for producing radioactive ions in flight. They enable us to access both the proton-rich and neutron-rich nuclei [1–7], which have attracted great interest in the frontier of nuclear physics. As

for applications, the spallation reaction can be used as a neutron source for nuclear energy generation and for nuclear waste transmutation in an accelerator-driven system (ADS) [8]. Therefore, having high-quality data for cross sections is essential for a systematic understanding of the spallation reaction processes as well as for improving theoretical models such that the required data can be calculated with high accuracy and reliability for both the research and application points of view.

The reaction mechanisms of the spallation reaction have been investigated by measuring the cross sections for many systems using different projectile-target combinations at various energies, such as  $^{137}\text{Cs} + p, d$  at 185 MeV/nucleon [9];  $^{107}\text{Pd} + p, d$  at 100 and 200 MeV/nucleon [10];  $^{93}\text{Zr} + p, d$  at 105 MeV/nucleon [11];  $^{56}\text{Fe} + p$  from 300 MeV/nucleon to

\* xhsun@pku.edu.cn

† Present address: Department of Physics, Tokyo Institute of Technology, 2-12-1 O-Okayama, Meguro, Tokyo 152-8551, Japan; wanghe@mail.nucl.ap.titech.ac.jp

‡ Present address: Photon Science Center, Graduate School of Engineering, University of Tokyo, Bunkyo-ku, Tokyo 113-8656, Japan.

1.5 GeV/nucleon [12]; and  $^{197}\text{Au} + p$  at 800 MeV/nucleon [13]. In particular, many experiments were performed to study the reactions of  $^{136}\text{Xe}$  [14–19], which is one of the most important nuclei to be used as a primary beam for the production of unstable nuclei. However, the studies have been mainly restricted to proton-induced reactions. For reactions induced by other targets, such as deuteron and heavy ions, experimental studies are scarce. Considering the importance for  $^{136}\text{Xe}$ , we measured systematically the spallation and fragmentation cross sections of  $^{136}\text{Xe}$  on proton, deuteron, and carbon targets at 168 MeV/nucleon. The newly obtained data, together with the previous ones in Refs. [15–18], can be used to systematically study the reaction mechanisms. In addition, the wide range of data for  $^{136}\text{Xe}$  play important roles in validating the theoretical calculations. For instance, the predictive power of different models for spallation reactions was discussed by comparing with the data for  $^{136}\text{Xe} + p$  at 1 GeV/nucleon [20]. This investigation should be helpful to assess various theoretical models and computing codes, which are widely needed not only in basic research but in many anticipated applications.

Since the direct measurement of the reaction products is important, the inverse kinematics technique was applied in this experiment. Namely,  $^{136}\text{Xe}$  was used as a projectile to bombard carbon, deuteron, and proton targets. As the reaction products are generated mainly at the forward angles in inverse kinematics, they were identified in flight by using the ZeroDegree spectrometer [21], and their cross sections can be directly obtained. The same method was previously used to measure the spallation reactions of  $^{137}\text{Cs}$  [9] and  $^{107}\text{Pd}$  [10] at 200 MeV/nucleon and  $^{93}\text{Zr}$  at 100 MeV/nucleon [11], which has demonstrated the validity of the inverse kinematics technique.

## II. EXPERIMENT

The experiment was performed at the Radioactive Isotope Beam Factory (RIBF), operated by RIKEN Nishina Center and the Center for Nuclear Study, University of Tokyo. The  $^{136}\text{Xe}$  data were obtained from the same experiment for  $^{137}\text{Cs}$  as reported in Ref. [9]. A  $^{238}\text{U}$  primary beam was accelerated to 345 MeV/nucleon, with an average beam intensity of approximately 12 pA. The secondary beams were produced via in-flight fission of  $^{238}\text{U}$  on a 1-mm-thick  $^9\text{Be}$  target, which was placed at the entrance of the BigRIPS separator [21]. The total intensities for the secondary beams were restricted by the requirements of the data acquisition system. The BigRIPS setting was tuned to select the  $N = 82$  isotones around  $^{136}\text{Xe}$  and  $^{137}\text{Cs}$ , as introduced in Ref. [9]. As  $^{136}\text{Xe}$  was provided as a secondary beam, both the beam energy and intensity were well determined by the BigRIPS separator. The particles in the secondary beams were identified event by event via the TOF- $B\rho$ - $\Delta E$  method [22]. The time of flight (TOF) was measured by two plastic scintillators. The magnetic rigidity ( $B\rho$ ) was determined by the trajectory reconstruction using the positions and angles of particles measured by parallel-plate avalanche counters (PPACs) installed along the beam line. The energy loss ( $\Delta E$ ) was measured by an ionization chamber. The atomic number,  $Z$ , and the mass-to-charge ratio,  $A/Q$ ,

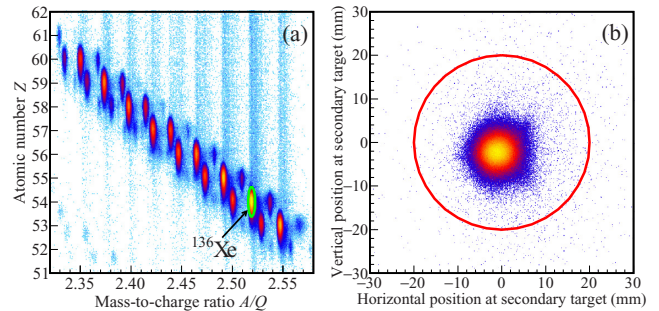


FIG. 1. (a) Two-dimensional particle identification plot of  $Z$  vs  $A/Q$  obtained from BigRIPS separator for secondary beams. The green circle indicates the selection for the incident  $^{136}\text{Xe}$  in the data analysis. (b) Beam profile of  $^{136}\text{Xe}$  on the secondary target. The red circle represents the real size of the secondary target.

were deduced from the TOF- $\Delta E$  and  $B\rho$ -TOF correlations, respectively. The particle identification plot for secondary beams in the BigRIPS separator are shown in Fig. 1(a). The resolutions in  $A/Q$  [given here as root mean square (rms)] and  $Z$  (rms) are  $1.1 \times 10^{-3}$  and 0.20, respectively. The typical intensity of  $^{136}\text{Xe}$  was  $1.6 \times 10^3$  particles per second (pps).

The secondary reactions for  $^{136}\text{Xe}$  projectile were induced by bombarding the  $\text{CH}_2$  (179.2 mg/cm $^2$ ),  $\text{CD}_2$  (217.8 mg/cm $^2$ ) [23], and  $^{12}\text{C}$  (226.0 mg/cm $^2$ ) targets, which are located at the entrance of the ZeroDegree spectrometer. The beam profile of  $^{136}\text{Xe}$  on the target, obtained from projecting the incident trajectories measured by the PPACs in front of the secondary target, is much smaller than the target size (40 mm in diameter), as can be seen in Fig. 1(b). The number of the incident  $^{136}\text{Xe}$  particles were then counted event by event according to the applied gates in Figs. 1(a) and 1(b) in the data analysis. The energy of the  $^{136}\text{Xe}$  beam was 168 MeV/nucleon in the center of the secondary targets. The target frame without material (empty target run) was used to subtract the background contribution.

The reaction products were analyzed by the ZeroDegree spectrometer [21]. The particles were identified event by event via the TOF- $B\rho$ - $\Delta E$  method, similar to the BigRIPS separator. The momentum acceptance of ZeroDegree spectrometer is  $\pm 3\%$ . The angular acceptances in the horizontal and vertical directions are  $\pm 45$  and  $\pm 30$  mrad, respectively. To cover a wide range of the products, several  $B\rho$  settings were applied for the ZeroDegree spectrometer:  $-9\%$ ,  $-6\%$ ,  $-3\%$ ,  $0\%$ , and  $+3\%$  relative to the  $B\rho$  value of the secondary beam.

Two-dimensional particle identification plots for reaction products produced from  $^{136}\text{Xe}$  in ZeroDegree spectrometer are displayed in Figs. 2(a) and 2(b). In Fig. 2(a), the plot combining all the  $B\rho$  settings is shown for  $^{136}\text{Xe}$  on carbon target. To demonstrate the identification for the reaction products in detail, the example for the  $-9\%$  setting for  $^{136}\text{Xe}$  on the  $\text{CD}_2$  target is displayed in Fig. 2(b). In order to show the statistics clearly, one-dimensional  $A/Q$  spectra for Xe (highest statistics) and Zr isotopes (lowest statistics) produced by  $^{136}\text{Xe}$  on C (blue line),  $\text{CD}_2$  (red line), and  $\text{CH}_2$  (black) targets are shown in Figs. 2(c) and 2(d), respectively. The typical  $A/Q$  (rms) and  $Z$  (rms) resolutions are  $2.5 \times 10^{-3}$  and

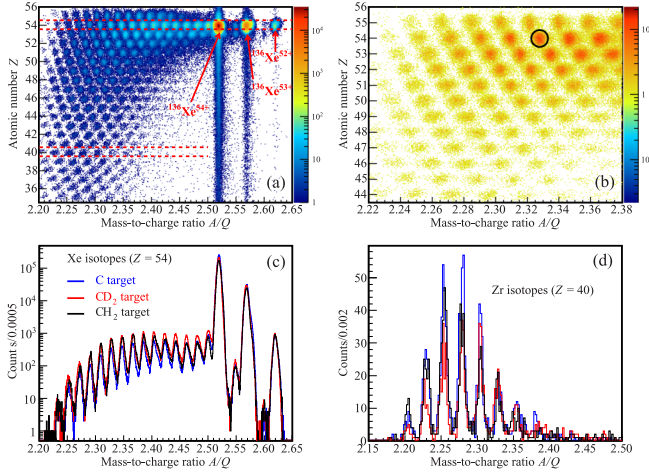


FIG. 2. (a) Two-dimensional particle identification plot of  $Z$  vs  $A/Q$  obtained from ZeroDegree spectrometer for the reaction products produced by  $^{136}\text{Xe}$  on carbon target, in combination of all the  $B\rho$  settings of  $+3\%$ ,  $0\%$ ,  $-3\%$ ,  $-6\%$ , and  $-9\%$ . The red dashed lines indicate the gate to select Xe and Zr isotopes. (b) The particle identification plot for the products produced from  $^{136}\text{Xe}$  on  $\text{CD}_2$  target with the  $-9\%$   $B\rho$  setting. The black circle indicates the  $^{126}\text{Xe}$  to guide the eye. (c) One-dimensional  $A/Q$  spectra for Xe isotopes produced by  $^{136}\text{Xe}$  on C (blue line),  $\text{CD}_2$  (red line), and  $\text{CH}_2$  (black) targets (achieved with highest statistics). (d) One-dimensional  $A/Q$  spectra for Zr isotopes produced by  $^{136}\text{Xe}$  on C (blue line),  $\text{CD}_2$  (red line), and  $\text{CH}_2$  (black) targets (achieved with lowest statistics).

0.30, respectively. The fraction of the fully stripped ( $Q = Z$ ) ions was approximately 66.0% for Xe isotopes transported through the ZeroDegree spectrometer for the reactions on the  $\text{CD}_2$  target. The GLOBAL code [24] was used to calculate the fraction of the fully stripped ions after traversing the ZeroDegree spectrometer and the calculation was verified by comparison of the calculated and experimental values for  $^{135}\text{Xe}$  and  $^{136}\text{Xe}$ . The H-like ( $Q = Z - 1$ ) ions were well identified and separated with the fully stripped ions. The contribution from the He-like ( $Q = Z - 2$ ) ions is less than 0.5%.

### III. RESULTS AND DISCUSSION

The cross sections on carbon ( $\sigma_C$ ),  $\text{CH}_2$  ( $\sigma_{\text{CH}_2}$ ), and  $\text{CD}_2$  ( $\sigma_{\text{CD}_2}$ ) were deduced from the measurement with C,  $\text{CH}_2$ , and  $\text{CD}_2$  targets after subtracting the contributions from the beam-line materials by using the data from empty target runs. The following formula was used to calculate the cross sections on carbon target:

$$\sigma_C = \frac{1}{A_C} \frac{1}{n_C} \left( \frac{Y_C}{I_C P_C} - \frac{Y_{\text{emp}}}{I_{\text{emp}} P_{\text{emp}}} \right), \quad (1)$$

where  $Y$  is the number of reaction products,  $n$  is the number of target nucleus per  $\text{cm}^2$ ,  $I$  is the number of the incident  $^{136}\text{Xe}$  particles,  $P$  is the ratio of the fully stripped ions, and  $A$  is the acceptance of the products in the ZeroDegree spectrometer. It is noted that the  $B\rho$  settings in ZeroDegree spectrometer enable the full acceptances ( $A = 100\%$ ) for most of the products. Only a few light-mass products with low momentum relative to the projectile were not fully accepted in the  $B\rho - 9\%$  setting. For these products, the acceptance ( $A$ )

was simulated by LISE++ [25] and applied to correct for the cross section. The cross sections on the proton target ( $\sigma_p$ ) were deduced by the formula:

$$\sigma_p = \frac{1}{2}(\sigma_{\text{CH}_2} - \sigma_C). \quad (2)$$

The same is true for the cross sections on deuteron target ( $\sigma_d$ ) just by replacing  $\text{CH}_2$  with  $\text{CD}_2$ .

#### A. Isotopic distribution of the cross section

The isotopic distributions of cross sections obtained in the present work for the reactions of  $^{136}\text{Xe} + \text{C}$ ,  $^{136}\text{Xe} + d$ , and  $^{136}\text{Xe} + p$  at 168 MeV/nucleon are plotted in Fig. 3. The error bars present the statistical uncertainties. The systematic uncertainties are estimated to be less than 12%, originating from the target thickness, the charge state distribution, and the acceptance of the ZeroDegree spectrometer. The contribution from the target thickness is less than 2% [9]. The uncertainties in charge state distributions are estimated to be less than 5% based on the GLOBAL code [24]. The uncertainties from the acceptance are estimated as less than 10% for the products with low momentum.

For the Cs isotopes that are produced by the charge-exchange or charge-pickup ( $\Delta Z = +1$ ) reactions,  $\sigma_C$  and  $\sigma_d$  are similar, as shown in Fig. 3(a). Both  $\sigma_C$  and  $\sigma_d$  are smaller than  $\sigma_p$  in the entire region of the Cs isotopic chain. The larger cross sections on the proton target than those on the deuteron target for charge-pickup reactions are also reported in studies of  $^{137}\text{Cs}$  and  $^{90}\text{Sr}$  at 185 MeV/nucleon [9] and  $^{93}\text{Zr}$  at 105 MeV/nucleon [11]. However, at 1 GeV/nucleon, the cross sections for the Cs isotopes produced in the reactions of  $^{136}\text{Xe} + \text{Be}$  [14] were found to be similar to those in  $^{136}\text{Xe} + p$  [15]. In addition, the cross sections for the charge-pickup reactions of  $^{208}\text{Pb}$  at 1 GeV/nucleon on proton and deuteron targets were found to be similar [28]. The differences in the observations among the examined reaction energies are caused by the contributions from the nucleon excitation component at higher energy [28]. The Xe and I isotopes are likely produced by the peripheral reactions [29], where the prefragments gain low excitation energy during the intranuclear cascade process, leading to a common shape of the isotopic distributions for all the three targets, namely the cross sections varying slightly over a wide range of mass numbers, as shown in Figs. 3(b) and 3(c). Furthermore, for Xe isotopes,  $\sigma_p$  and  $\sigma_d$  have similar values, and both of them are larger than  $\sigma_C$ . For I isotopes,  $\sigma_d$  becomes the largest. The isotopic distributions show a bell-like shape for other elements with the atomic number  $Z < 53$ . However, the position of the maximum cross section differs among the three targets and is on the more neutron-deficient side for carbon target than for proton and deuteron targets. The peak position depends on the neutron-proton evaporation competition during the deexcitation stage [7]. For the reactions induced by all these three targets at 168 MeV/nucleon, the excitation energies gained by the prefragments are not sufficient to reach the evaporation corridor [7]. The relatively higher excitation energy in the carbon-induced reactions leads to more neutrons being evaporated. From Te to Cd, a strong target dependence is found. As presented in Figs. 3(d)–3(h),  $\sigma_d$  and  $\sigma_C$  are close

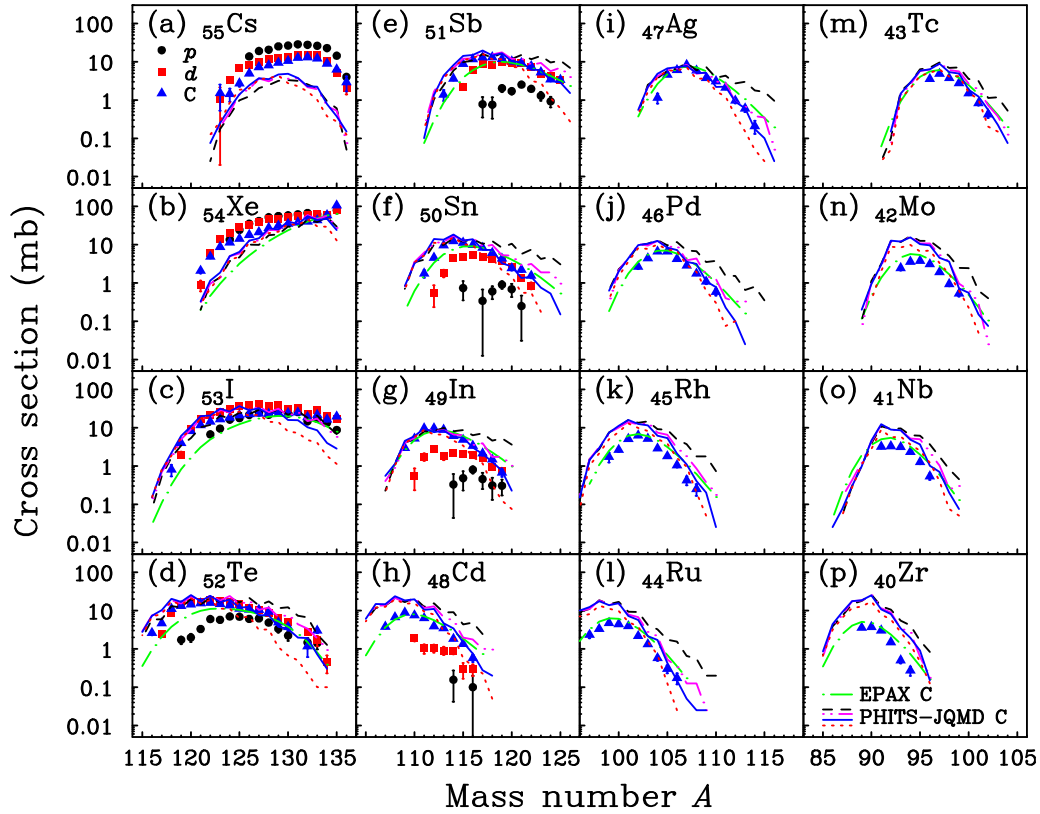


FIG. 3. Isotopic distributions of the cross sections for the products that are produced in the reactions of  $^{136}\text{Xe} + p$  (filled circle),  $^{136}\text{Xe} + d$  (filled square), and  $^{136}\text{Xe} + \text{C}$  (filled triangle) at 168 MeV/nucleon. The error bars correspond to the statistical uncertainties. The EPAX [26] (green dot-dashed lines) and PHITS-JQMD [27] calculations on carbon target are plotted for comparison. The PHITS-JQMD calculations using JQMD + GEM models are made with different switching times of 150 (black dashed lines), 100 (magenta dot-dot-dashed lines), 75 (blue solid lines), and 50 fm/c (red dotted lines).

to each other on the neutron-rich side and both of them are larger than  $\sigma_p$ . While for the neutron-deficient side,  $\sigma_p$  drops more quickly than  $\sigma_d$  and  $\sigma_C$ . As a result,  $\sigma_C$  becomes much larger than both of  $\sigma_d$  and  $\sigma_p$ , in particular when the number of nucleons removed from  $^{136}\text{Xe}$  exceeds 20. These nuclei are produced most likely by central collisions [30] and the production cross sections depend on the excitation energies gained by the prefragments during the intranuclear cascade stage. Higher excitation energy gained by the prefragments is correlated with longer evaporation chains and thus leads to larger cross sections for isotopes far away from the projectile. It is evident that, for the production of neutron-deficient isotopes far away from the projectile, the carbon target has the obvious advantage of higher production power.

It would be interesting to check  $\sigma_d$  for more details. As displayed in Figs. 3(b) and 3(c),  $\sigma_d$  is larger than  $\sigma_C$  for Xe and I isotopes in general. This finding suggests that the deuteron target may be used to populate the entire chain of isotopes very close to the projectile with a potential comparable to or even higher than heavier targets. Previously,  $\sigma_d$  was found to be larger than those on  $^9\text{Be}$  and  $^{181}\text{Ta}$  targets for few-nucleon removal reactions in the fragmentation of  $^{48}\text{Ca}$  [32] at 100 MeV/nucleon, which could be attributed to the contributions from both the nondissipative process and statistical mechanisms. Moreover, for neutron-rich products, larger  $\sigma_d$  than  $\sigma_C$  are found for Te isotopes, and similar values between

$\sigma_d$  and  $\sigma_C$  are found for Sb, Sn, and In isotopes, as can be seen in Figs. 3(d)–3(g). For the fragmentation of  $^{136}\text{Xe}$  at higher reaction energies, larger cross sections on the deuteron target were found for the production of neutron-rich I and Te isotopes at 500 MeV/nucleon [16], in comparison to those on  $^9\text{Be}$  target at 1 GeV/nucleon [14]. Cross sections for  $^{136}\text{Xe} + d$  at 500 MeV/nucleon are even comparable to those for  $^{136}\text{Xe} + ^{208}\text{Pb}$  at 1 GeV/nucleon [19]. All these measurements demonstrate that deuteron target has an advantage over heavy targets for the production of the neutron-rich nuclei and near-projectile isotopic chains.

### B. Comparison with model calculation

To have a more quantitative understanding of the experimental results, the newly measured data are compared with both theoretical calculations and empirical parametrizations. The carbon-target data are compared with theoretical calculations including both the dynamical and evaporation processes implemented in Particle and Heavy Ion Transport code System (PHITS) 3.17, denoted as PHITS-JQMD. The dynamical process is made by using the JAERI quantum molecular dynamics model (JQMD) [33], which is widely used to analyze various aspects of the reactions induced by heavy ions. The present calculation uses JQMD-2.0 [34], which is the modified version of JQMD for a better

description of the peripheral reactions by revising the Hamiltonian with the relativistic covariance and the neutron-proton scattering cross section at the nuclear surface. The evaporation process is described by the generalized evaporation model (GEM) [35], which is based on the Weisskopf-Ewing formalism.

The JQMD calculation is connected to the GEM at a certain timescale, namely the switching time  $t_{sw}$ , which affects the reaction cross sections. According to Refs. [33,36,37], the switching time depends on both the incident energy and the combination of projectile and target. The  $t_{sw}$  values between 100 and 150 fm/c were once suggested to the reactions of  $^{208}\text{Pb} + p$  at 1.5 GeV/nucleon [33] and  $^{nat}\text{Pb} + ^{12}\text{C}$  at 400 MeV/nucleon [36]. In order to investigate the  $t_{sw}$  dependence of  $\sigma_C$ , the PHITS-JQMD calculations were performed with different switching times of 150 (black dashed lines), 100 (magenta dot-dot-dashed lines), 75 (blue solid lines), and 50 fm/c (red dotted lines), as shown in Fig. 3. For I isotopes, the results with 100- and 150-fm/c switching times show a reasonable agreement with the experimental data as presented in Fig. 3(c). From Te to Pd, as shown in Figs. 3(d)–3(j), the cross sections for the isotopes on the neutron-rich side were overestimated with the switching times of 100 and 150 fm/c while underestimated with 50 fm/c. Such  $t_{sw}$  dependence could be tentatively interpreted as following. With a longer switching time, more excitation energy can be taken away by the emission of nucleons (both protons and neutrons) in the dynamical process. Thus, the excitation energy of the prefragment becomes lower, resulting in larger yields for the neutron-rich isotopes [36]. In contrast, a shorter switching time leads to a prefragment with higher excitation energy followed by more neutron evaporation, resulting in smaller yields of the neutron-rich isotopes. In general, the PHITS-JQMD calculations with  $t_{sw} = 75$  fm/c show better agreement with the experimental results for the isotopes on the neutron-rich side for  $Z < 52$ . On the other hand, the cross sections for isotopes on the neutron-deficient side are not sensitive to the switching time. These isotopes are mainly produced from central collisions followed by the evaporation process, in which a proton is more likely to be emitted than a neutron. The present study with respect to the new data on carbon target reveals the necessity to further investigate the switching time when applying the PHITS-JQMD code.

The cross sections on carbon target are also compared with empirical parametrization of fragmentation cross sections (EPAX) [26], which is widely used to estimate the yield for secondary beam production. Underestimation on the neutron-deficient side was observed for the Xe, I, and Te isotopes. Such underestimation was previously found in the reaction of  $^{86}\text{Kr} + ^9\text{Be}$  at 64 MeV/nucleon [38] and  $^{48}\text{Ca} + ^9\text{Be} / ^{181}\text{Ta}$  at 140 MeV/nucleon [39]. Satisfactory reproduction of the experimental results is realized by the EPAX calculations for the isotopes with the atomic number  $Z < 52$ . However, overestimated cross sections appear at the neutron-rich side. Indeed, as shown in Ref. [14] for  $^{136}\text{Xe} + ^9\text{Be}$  at 1 GeV/nucleon, EPAX overestimates the cross section on the neutron-rich side and the discrepancy increases with the decreasing proton number. It is evident that the actual EPAX parametrization needs to be optimized according to the expanded data sets.

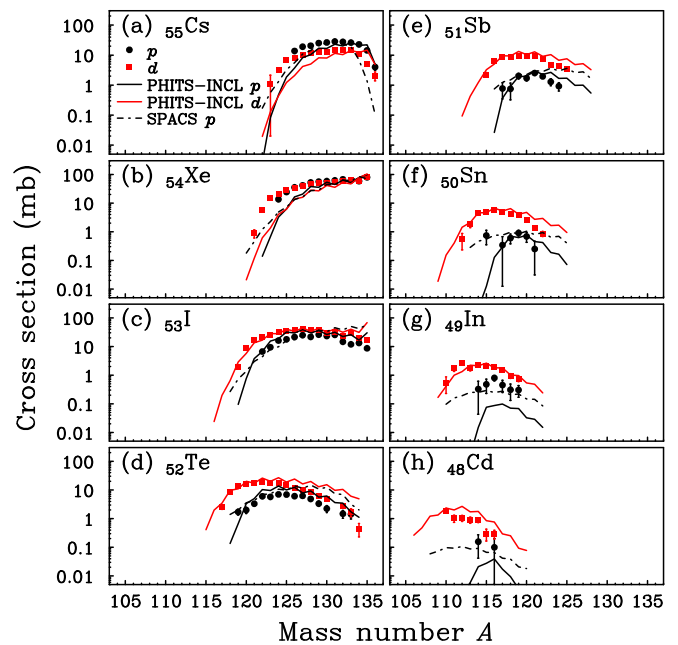


FIG. 4. Same as Fig. 3, but for the data on proton (filled circle) and deuteron (filled square) targets. The solid lines correspond to the PHITS-INCL calculations [27] on proton (black) and deuteron (red) targets and the dot-dashed lines correspond to the SPACS [31] calculations on the proton target.

Analysis of data on proton and deuteron targets uses a theoretical code different from that for heavy-ion collisions. In the present work, the calculations by PHITS (denoted as PHITS-INCL) including cascade and evaporation processes are performed, as displayed in Fig. 4. These two processes are described by the intranuclear cascade model of Liege (INCL, version 4.6) [41] and GEM [35], respectively. INCL is a microscopic model that gives a good description of nucleon- and light-particle-induced reactions at relative high energies. In the INCL approach, the nucleon-nucleon collisions are considered as a succession of binary collisions and the particles travel along straight-line trajectories. The stopping time from cascade process to evaporation process is determined self-consistently [41]. As displayed in Fig 4, The PHITS-INCL calculations describe well the general trend of experimental data for proton and deuteron targets. However, for the neutron-rich isotopes of Te, Sb, and Sn, the overestimation of the cross sections can be seen from Figs. 4(d)–4(f). For the one-nucleon removal channels of  $^{135}\text{Xe}$  and  $^{135}\text{I}$ , PHITS-INCL calculations overestimate the cross sections. Such overestimation was also observed for  $^{93}\text{Zr}$  at 105 MeV/nucleon [11]. As described in Ref. [42], the calculation for the one-nucleon-removal channel could be improved by introducing the neutron skin and fuzzy initial conditions. In addition, the even-odd staggering is overestimated in both the PHITS-JQMD and PHITS-INCL calculations. As discussed in Refs. [31,43], this overestimation may be due to the competition between particle evaporation and  $\gamma$ -ray emission in the evaporation process and the influence of angular momentum in level density that used in GEM. It is clear that PHITS-INCL is generally applicable but some fine adjustments are still needed for certain range of isotopes.

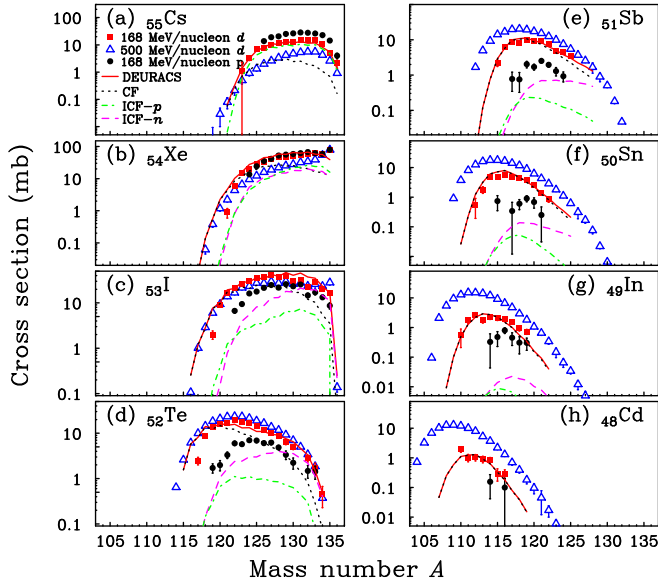


FIG. 5. Isotopic distributions of the cross sections for the products produced in the reactions of  $^{136}\text{Xe} + d$  at different reaction energies. The red squares represent the cross sections obtained from this work at 168 MeV/nucleon. The blue triangles represent the cross sections at 500 MeV/nucleon [16]. The solid lines represent the results of the DEURACS [40] calculations for  $^{136}\text{Xe} + d$  at 168 MeV/nucleon, which are the sum of the three components, absorption of deuteron (CF, black dotted lines), absorption of breakup proton (ICF- $p$ , green dot-dashed lines), and absorption of breakup neutron (ICF- $n$ , magenta dashed lines). The cross sections for the reactions of  $^{136}\text{Xe} + p$  at 168 MeV/nucleon (filled circles) were also plotted for comparison. The error bars represent the total uncertainty (statistical and systematic).

The cross sections on proton target were also compared with the semi-empirical parametrization for residue cross sections in spallation reactions (SPACS) [31], which is developed to describe the proton- and neutron-induced spallation reactions. Isotopic cross sections for I and Sb produced in  $^{136}\text{Xe} + p$  at 200 MeV/nucleon were once compared with SPACS, showing a reasonable agreement as reported in Ref. [31]. The present work extends the comparison for other isotopes from Cs to Cd as shown in Fig. 4. Overall, the shape of the isotopic distribution from I to Cd is well reproduced by SPACS calculation, except the overestimation on the neutron-rich side of Te, Sb, and Sn isotopes, as shown in Figs. 4(d)–4(f).

We further investigated the deuteron-target results with the newly developed deuteron-induced reaction analysis code system (DEURACS) [40], which explicitly takes the breakup process of deuteron into consideration. As shown in Fig. 5, a good agreement with the experimental data is achieved. In DEURACS, the calculated cross sections can be decomposed into three components: the absorption of the breakup proton [incomplete fusion of proton (ICF- $p$ )], the absorption of the breakup neutron [incomplete fusion of neutron (ICF- $n$ )], and the absorption of the entire deuteron [complete fusion of deuteron (CF)]. As shown in Fig. 5(a), the production of the Cs isotopes is dominated by the ICF- $p$  component, being

consistent with the results of  $^{93}\text{Zr}$  at 100 MeV/nucleon and  $^{107}\text{Pd}$  at 100 and 196 MeV/nucleon [40]. The contributions from the breakup proton are comparable to those from the breakup neutron for Xe isotopes, as shown in Fig. 5(b). On the other hand, ICF- $n$  gives clearly larger contributions than ICF- $p$  for neutron-rich isotopes with  $Z < 54$ . For the products with more than 14 nucleons removed from  $^{136}\text{Xe}$ , such as those on the neutron-deficient side of the isotopic chains from I to Cd, CF component is predominant. As mentioned above, a higher excitation energy is required for the production of these light-mass products. In the CF process, both proton and neutron contribute to the reactions, and thus introduce more energy into the prefragments. The satisfactory reproduction of DEURACS demonstrates the importance of the breakup process in deuteron-induced reactions, especially for isotopes close to the projectile.

The higher cross sections on the deuteron target than those on the proton target for the neutron-rich isotopes close to  $^{136}\text{Xe}$  can be explained with DEURACS calculations. As shown in Figs. 5(c) and 5(d), the ICF- $n$  component gives larger contributions than ICF- $p$ , and even larger than  $\sigma_p$  for the neutron-rich sides of I and Te isotopes, resulting in larger  $\sigma_d$  than  $\sigma_p$ .

### C. Energy dependence investigation

To investigate the energy dependence of the reactions, the cross sections for  $^{136}\text{Xe} + d$  at 168 and 500 MeV/nucleon [16] are compared, as shown in Fig. 5. The cross sections for the Cs isotopes at 168 MeV/nucleon are approximately twice those at 500 MeV/nucleon, as displayed in Fig. 5(a). Energy dependence for the charge-exchange or charge-pickup reactions in which the cross sections decrease with increasing reaction energy from 100 to 1000 MeV/nucleon was reported in Refs. [44,45]. Cross sections at 168 MeV/nucleon are larger than those at 500 MeV/nucleon for the Xe isotopes, as shown in Fig. 5(b), except for  $^{135}\text{Xe}$ . For  $^{135}\text{Xe}$  produced by one neutron removal from the  $^{136}\text{Xe}$  projectile, the cross sections are similar at these two energies. As discussed in Ref. [46], the production cross section of the one-neutron-removal reaction for  $^{197}\text{Au} + p$  system was found to remain constant above 200 MeV/nucleon, which is characteristic of the peripheral reactions. The cross sections for I isotopes are similar at these two energies. For the isotopic chains with  $Z < 53$ , the cross sections at 168 MeV/nucleon become smaller than those at 500 MeV/nucleon. The comparison between 168 and 500 MeV/nucleon further indicates higher excitation energy of the prefragments, leading to larger cross sections of the light products far away from the projectile.

The cross sections for the reactions of  $^{136}\text{Xe} + p$  at 168, 200 [18], 500 [17], and 1000 MeV/nucleon [15] are presented in Fig. 6 to exhibit the energy dependence of  $\sigma_p$ . As can be seen from Figs. 6 and 5, the energy dependence of  $\sigma_p$  is similar to that of  $\sigma_d$ . For the Cs and Xe isotopes, the cross sections decrease with the increasing reaction energy. In contrast, for the isotopes with  $Z < 53$ , the cross sections at higher reaction energy become larger due to the induced higher excitation energy of the prefragments, consistent with that observed in the deuteron-target data.

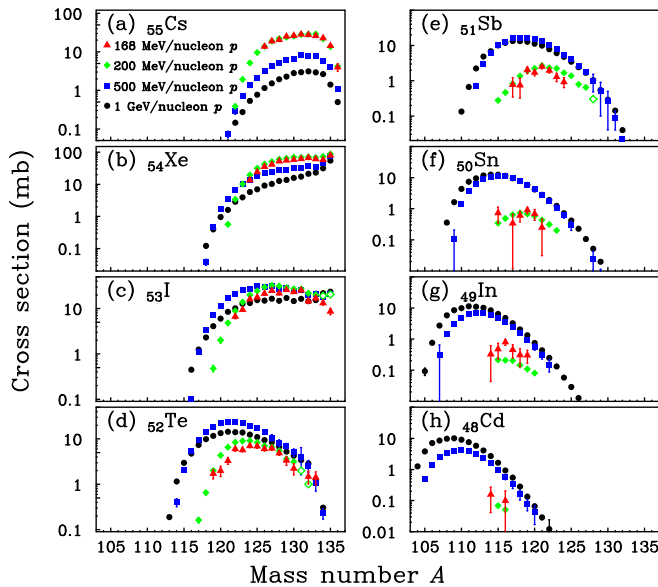


FIG. 6. Isotopic distributions of the cross sections in the reactions of  $^{136}\text{Xe} + p$ . The red triangles represent cross sections obtained in the present work at 168 MeV/nucleon. The green diamonds, blue squares, and black dots represent the cross sections at 200 [18], 500 [17], and 1000 MeV/nucleon [15], respectively. The open points at 200 MeV/nucleon represent the extrapolated values [18]. The error bars represent the total uncertainty (statistical and systematic).

#### D. Mass distribution of the cross section

In order to have an overview of the target and energy dependence of the production cross sections, the mass distribution of the cross sections is plotted in Fig. 7. The cross sections on different targets at 168 MeV/nucleon are compared in Fig. 7(a). Because of the limited  $B\rho$  settings, the cross sections of the very light-mass products for carbon target were not measured. For the products close to  $^{136}\text{Xe}$  ( $A > 125$ ),  $\sigma_p$  and  $\sigma_d$  are almost equal, and both remain almost constant and larger than  $\sigma_C$  except for  $A = 135$ . With decreasing mass number, both  $\sigma_p$  and  $\sigma_d$  decrease more rapidly than that for  $\sigma_C$ . For the products far away from  $^{136}\text{Xe}$  ( $A < 120$ ),  $\sigma_C$  becomes larger than  $\sigma_p$  and  $\sigma_d$ . As discussed above, this can be explained by the differences in excitation energy of the prefragments induced by different targets. The higher excitation energy in carbon-induced reactions results in wider coverage on the mass distribution.

The experimental mass distributions are also compared with the PHITS and EPAX calculations, as shown in Fig. 7(a). The PHITS-INCL calculations reproduce well the general trend of the mass distribution for proton and deuteron targets. For the carbon-target results, the EPAX calculations underestimate the cross sections for products with  $A > 115$  because of the lack of calculations for Cs isotopes and the underestimated cross sections for Xe isotopes, as shown in Figs. 3(a) and 3(b). For the products with mass number  $A < 115$ , the difference between the EPAX results and the experimental data is less than 5 mb. For the description of the carbon-target data, the switching time of PHITS-JQMD calculations does not affect significantly the overall mass distribution. The calculations

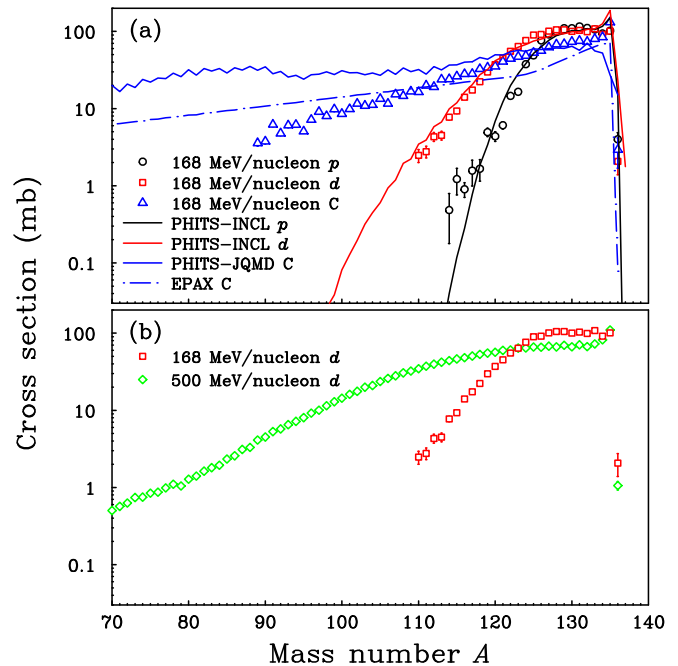


FIG. 7. Mass distributions of the cross sections for the products produced in the reactions of  $^{136}\text{Xe} + p$  (black circle),  $^{136}\text{Xe} + d$  (red square), and  $^{136}\text{Xe} + C$  (blue triangle) at 168 MeV/nucleon. The PHITS-INCL [27] calculations on proton and deuteron are presented by the black solid line and red solid line, respectively. The EPAX [26] calculations on carbon are presented by the dot-dashed line. The PHITS-JQMD calculations on carbon with switching time of 75 fm/c are presented by the blue solid line. (b) The mass distributions of the cross sections for the products produced in the reactions of  $^{136}\text{Xe} + d$  at 168 MeV/nucleon (red squares) and 500 MeV/nucleon (green diamonds) [16].

with switching times of 75 fm/c are shown in Fig. 7(a). The calculations underestimate the production cross sections of the heavy-mass products due to the underestimation for the Cs and Xe isotopes, as shown in Figs. 3(a) and 3(b). For light-mass products, PHITS-JQMD overestimate the cross sections.

To gain further insight on the effect of the excitation energy, the mass distributions of the cross sections on deuteron target at 168 and 500 MeV/nucleon are presented in Fig. 7(b). The cross sections at these two energies remain almost constant for the products close to the projectile. The corresponding flat region at 500 MeV/nucleon is wider than that at 168 MeV/nucleon. For these near-projectile products, the cross sections at 168 MeV/nucleon are higher than those at 500 MeV/nucleon due to larger productions of Cs and Xe isotopes, as shown in Figs. 5(a) and 5(b). With the decreasing mass number, the cross sections at 168 MeV/nucleon decrease more rapidly than those at 500 MeV/nucleon, with a crossing appearing at about  $A = 126$ . Again, the differences in shape of the mass distribution at 168 and 500 MeV/nucleon show that higher excitation energy of the prefragments is in favor of the production of isotopes far away from the projectile.

TABLE I. Total cross sections measured in the present work on proton and deuteron targets at 168 MeV/nucleon, to be compared with PHITS calculations. The numbers in the first and second parentheses represent the statistical and the systematical uncertainties, respectively.

Reaction	$\sigma_{\text{EXPint}}$ (mb)	$\sigma_{\text{PHITSacc}}$ (mb)	$\sigma_{\text{PHITStot}}$ (mb)
$^{136}\text{Xe} + p$	1161 (8)(11)	1159	1188
$^{136}\text{Xe} + d$	1486 (7)(12)	1527	1596

### E. Total reaction cross section

The integral total cross sections on proton and deuteron targets were listed in Table I, where  $\sigma_{\text{EXPint}}$  refers to the integration of the measured isotopic cross sections in Fig. 3. The total cross section on carbon target is not listed due to the lack of some isotope measurement caused by the limited  $B\rho$  settings, as mentioned above. The total cross sections calculated by PHITS were also listed in Table I for comparison.  $\sigma_{\text{PHITSacc}}$  represents the integration of only the calculated production cross sections that can be obtained from the experiment.  $\sigma_{\text{PHITStot}}$  represents the integration of all the production cross sections calculated by PHITS. The calculations agree well with the experimental results on proton and deuteron targets for the total cross sections.

### IV. SUMMARY

In summary, the cross sections for the spallation and fragmentation reactions of  $^{136}\text{Xe}$  on carbon, deuteron, and proton targets at 168 MeV/nucleon have been measured via inverse kinematics using the BigRIPS separator and ZeroDegree spectrometer. The newly obtained data for the carbon target allows us to explore the possibilities of new isotope production and to investigate the reaction mechanisms. We have shown that, for the production of light-mass isotopes far away from the projectile, the carbon target has clearly higher potential in comparison to proton or deuteron targets. This advantage is attributed to the possible higher excitation energies induced by heavier targets. Based on the data obtained from the carbon target, theoretical calculations in the framework of heavy-ion transportation, using the JQMD + GEM code, are performed and compared with data for 16 isotopic chains. The calculations reproduce the general trend for isotopic chains of  $Z = 53\text{--}49$  well, but overestimate the cross sections for isotopic chains far away from the projectile with  $Z < 49$ . Furthermore, the calculated production yields on the neutron-rich side are quite sensitive to the switching-time parameter, which needs to be further investigated in the future based on measurements with more energy-target combinations. The deuteron target has been studied in detail, thanks to the measurement of eight isotopic chains and the theoretical calculations with the transport code (INCL + GEM) and also the code incorporating the breakup effect (DEURACS). It is demonstrated that the deuteron target has advantages to produce isotopic chains very close to the projectile and also the neutron-rich nuclei in other isotopic chains far away from the projectile. This may be attributed to its weakly bound property and the strong effect

of the breakup neutron in the peripheral collision processes. The data from the proton target serve as a benchmark for the validity of the present measurement since a lot of results on protons at various energies are available in the literature. The proton target has the advantage of producing isotopes by charge-pickup reactions in comparison to deuteron and heavier targets. In general, proton-target data can be well described by the INCL + GEM calculations. Combining with experimental results from previous measurements on proton and deuteron targets at various energies, target and energy dependences of the fragment-mass distribution have been investigated. It is evident that the higher excitation energy of the prefragment is in favor of the production of isotopes far away from the projectile. The present systematic analysis would serve as a useful ground for further measurements and code improvements regarding to the importance of spallation and fragmentation reactions.

### ACKNOWLEDGMENTS

We express our gratitude to the accelerator staff of the RIKEN Nishina Center for providing the  $^{238}\text{U}$  beam. This work is supported by the grant MEXT Nuclear System Research and Development Program. One of the authors (H.W.) acknowledges the support from MEXT KAKENHI Grants No. 18H05404.

### APPENDIX

Isotopic cross sections for the products produced in the reactions of  $^{136}\text{Xe}+p$ ,  $^{136}\text{Xe}+d$ , and  $^{136}\text{Xe}+C$  at 168 MeV/nucleon are shown in Table II.

TABLE II. Isotopic cross sections for the products produced in the reactions of  $^{136}\text{Xe}$  on proton, deuteron, and carbon at 168 MeV/u. The numbers in parentheses represent the statistical uncertainty. The systematic uncertainties are estimated to be less than 12%.

$Z$	$A$	$\sigma_c$ (mb)	$\sigma_d$ (mb)	$\sigma_p$ (mb)
55	136	2.9(1.2)	2.1(0.7)	4.0(0.9)
55	135	6.3(0.6)	5.2(0.4)	14.4(0.6)
55	134	8.9(0.7)	10.5(0.6)	22.7(0.8)
55	133	12.2(0.8)	14.7(0.7)	26.0(0.9)
55	132	13.1(0.6)	15.0(0.5)	27.7(0.9)
55	131	12.7(0.6)	14.5(0.5)	28.5(0.6)
55	130	10.6(0.6)	13.0(0.5)	26.4(0.6)
55	129	9.4(0.5)	12.4(0.5)	25.1(0.6)
55	128	8.1(0.7)	11.5(0.6)	20.5(0.7)
55	127	7.2(0.6)	10.1(0.6)	19.0(0.6)
55	126	4.9(0.5)	8.0(0.5)	13.7(0.5)
55	125	2.7(0.5)	6.8(0.5)	
55	124	1.4(0.5)	3.3(0.5)	
55	123	1.5(1.0)	1.1(1.1)	
54	135	106.2(4.2)	79.4(2.9)	79.2(3.5)
54	134	59.1(3.3)	59.7(2.3)	58.0(2.8)
54	133	43.5(1.5)	61.9(1.2)	61.7(1.4)
54	132	40.3(1.5)	58.7(1.3)	67.2(1.6)
54	131	38.2(1.5)	56.1(1.2)	62.0(1.5)
54	130	35.2(1.4)	52.1(1.2)	58.4(1.5)



TABLE II. (Continued).

TABLE II. (Continued).					TABLE II. (Continued).				
Z	A	$\sigma_c$ (mb)	$\sigma_d$ (mb)	$\sigma_p$ (mb)	Z	A	$\sigma_c$ (mb)	$\sigma_d$ (mb)	$\sigma_p$ (mb)
					51	116	11.7(0.6)	6.3(0.5)	
54	129	31.5(1.0)	48.4(0.8)	55.8(0.9)	51	115	8.7(0.5)	2.2(0.4)	
54	128	27.6(0.9)	47.9(0.8)	52.3(0.9)	51	114	3.6(0.4)		
54	127	21.4(0.9)	40.1(0.7)	41.4(0.8)	51	113	1.4(0.4)		
54	126	18.1(1.1)	33.4(1.0)	35.3(0.9)	50	122	1.6(0.2)	0.9(0.2)	
54	125	14.4(0.9)	29.1(0.9)	24.2(0.8)	50	121	2.2(0.3)	1.4(0.2)	0.3(0.2)
54	124	11.4(0.8)	20.5(0.7)	13.5(0.6)	50	120	2.4(0.3)	2.7(0.3)	0.7(0.3)
54	123	8.7(0.6)	14.5(0.6)		50	119	4.4(0.3)	3.8(0.2)	0.9(0.2)
54	122	4.9(0.4)	5.9(0.4)		50	118	6.1(0.3)	4.3(0.3)	0.6(0.2)
54	121	2.1(0.3)	0.9(0.3)		50	117	8.3(0.5)	4.8(0.4)	0.3(0.3)
53	135	19.6(1.4)	16.7(1.1)	8.7(1.2)	50	116	9.9(0.5)	5.5(0.4)	
53	134	16.5(1.8)	20.6(1.3)	13.3(1.2)	50	115	11.3(0.5)	4.8(0.4)	0.7(0.4)
53	133	21.6(1.7)	29.4(1.7)	17.1(1.8)	50	114	12.4(0.5)	4.6(0.5)	
53	132	19.0(1.8)	22.4(1.3)	14.6(1.5)	50	113	9.6(0.5)	1.8(0.4)	
53	131	25.0(1.1)	32.4(0.8)	25.5(1.7)	50	112	4.6(0.4)	0.6(0.3)	
53	130	24.1(0.9)	29.9(0.8)	23.3(0.9)	50	111	1.8(0.4)		
53	129	23.2(1.0)	38.1(0.9)	25.9(1.0)	49	119	0.7(0.2)	0.7(0.1)	0.3(0.1)
53	128	23.0(1.0)	36.8(0.9)	21.7(1.0)	49	118	1.5(0.2)	1.0(0.2)	0.3(0.2)
53	127	23.2(0.7)	40.5(0.7)	24.8(0.7)	49	117	2.1(0.2)	1.6(0.2)	0.5(0.2)
53	126	22.6(0.7)	37.9(0.7)	21.5(0.7)	49	116	3.4(0.2)	1.9(0.2)	0.8(0.2)
53	125	21.2(0.7)	35.8(0.7)	17.8(0.6)	49	115	4.8(0.4)	2.0(0.3)	0.5(0.3)
53	124	18.4(0.9)	31.1(0.9)	16.1(0.7)	49	114	6.1(0.4)	2.2(0.3)	0.3(0.3)
53	123	16.7(0.8)	25.6(0.8)	9.4(0.6)	49	113	8.8(0.5)	1.8(0.4)	
53	122	14.3(0.7)	21.5(0.7)	6.7(0.6)	49	112	9.6(0.5)	2.7(0.4)	
53	121	11.7(0.7)	16.8(0.7)		49	111	9.6(0.5)	1.7(0.4)	
53	120	8.2(0.6)	9.2(0.5)		49	110	5.2(0.4)	0.6(0.3)	
53	119	4.0(0.4)	2.0(0.4)		49	109	3.0(0.4)		
53	118	0.8(0.3)			48	116	0.6(0.1)	0.3(0.1)	0.1(0.1)
52	134		0.5(0.2)		48	115	1.4(0.2)	0.3(0.1)	
52	133	3.0(0.5)	1.7(0.5)	1.4(0.5)	48	114	1.8(0.2)	0.9(0.2)	0.2(0.1)
52	132	1.2(0.6)	2.8(0.5)	1.5(0.5)	48	113	3.5(0.3)	0.9(0.2)	
52	130	3.8(0.7)	5.0(0.6)	2.2(0.6)	48	112	3.9(0.3)	1.0(0.3)	
52	129	4.9(0.8)	6.3(0.6)	3.4(0.7)	48	111	6.4(0.4)	1.0(0.3)	
52	128	9.3(0.5)	8.5(0.4)	4.9(0.5)	48	110	7.6(0.4)	1.9(0.3)	
52	127	10.5(0.5)	10.3(0.5)	6.2(0.5)	48	109	8.9(0.5)		
52	126	10.7(0.6)	11.9(0.5)	6.1(0.6)	48	108	6.7(0.4)		
52	125	11.3(0.6)	14.6(0.6)	6.9(0.6)	48	107	3.8(0.4)		
52	124	13.8(0.5)	17.1(0.5)	7.0(0.4)	47	114	0.2(0.1)		
52	123	14.9(0.5)	18.1(0.5)	5.7(0.4)	47	113	0.6(0.1)		
52	122	16.1(0.7)	19.4(0.7)	6.0(0.6)	47	112	1.0(0.2)		
52	121	15.5(0.7)	16.9(0.7)	3.3(0.5)	47	111	2.1(0.2)		
52	120	14.5(0.7)	15.8(0.7)	2.0(0.5)	47	110	3.1(0.2)		
52	119	13.3(0.8)	13.7(0.6)	1.7(0.4)	47	109	3.8(0.3)		
52	118	11.2(0.6)	8.7(0.5)		47	108	5.9(0.4)		
52	117	4.7(0.4)	2.5(0.4)		47	107	8.3(0.4)		
52	116	2.6(0.4)			47	106	6.1(0.4)		
51	125	3.4(0.3)	3.4(0.3)		47	105	4.6(0.4)		
51	124	3.5(0.4)	4.3(0.3)	0.9(0.3)	47	104	1.1(0.3)		
51	123	5.3(0.4)	4.7(0.4)	1.3(0.3)	46	110	0.6(0.1)		
51	122	7.7(0.3)	7.4(0.3)	2.0(0.3)	46	109	1.1(0.2)		
51	121	9.2(0.4)	9.3(0.3)	2.5(0.3)	46	108	1.8(0.2)		
51	120	10.1(0.4)	9.3(0.4)	1.7(0.3)	46	107	2.8(0.2)		
51	119	11.8(0.6)	9.6(0.5)	2.0(0.4)	46	106	4.3(0.3)		
51	118	13.1(0.6)	8.4(0.5)	0.8(0.4)	46	105	6.7(0.4)		
51	117	13.1(0.8)	8.5(0.5)	0.8(0.4)	46	104	6.7(0.4)		

TABLE II. (*Continued*).

Z	A	$\sigma_C$ (mb)	$\sigma_d$ (mb)	$\sigma_p$ (mb)
46	103	4.4(0.3)		
46	102	2.7(0.4)		
45	108	0.3(0.1)		
45	107	0.4(0.1)		
45	106	1.0(0.1)		
45	105	1.8(0.2)		
45	104	2.9(0.2)		
45	103	5.2(0.3)		
45	102	6.3(0.3)		
45	101	5.1(0.3)		
45	100	2.6(0.3)		
45	99	1.7(0.5)		
44	106	0.2(0.1)		
44	105	0.3(0.1)		
44	104	0.6(0.1)		
44	103	1.3(0.1)		
44	102	2.2(0.2)		
44	101	3.9(0.3)		
44	100	4.4(0.3)		
44	99	4.8(0.3)		
44	98	3.3(0.3)		
44	97	2.3(0.4)		
43	102	0.4(0.1)		
43	101	0.8(0.1)		

TABLE II. (*Continued*).

Z	A	$\sigma_C$ (mb)	$\sigma_d$ (mb)	$\sigma_p$ (mb)
43	100	1.5(0.2)		
43	99	2.8(0.2)		
43	98	3.7(0.3)		
43	97	4.9(0.3)		
43	96	3.6(0.3)		
42	99	0.5(0.1)		
42	98	0.9(0.1)		
42	97	1.9(0.2)		
42	96	3.1(0.2)		
42	95	3.8(0.3)		
42	94	3.6(0.3)		
42	93	2.5(0.3)		
41	96	0.5(0.1)		
41	95	1.3(0.2)		
41	94	2.3(0.2)		
41	93	3.1(0.2)		
41	92	3.3(0.3)		
41	91	3.2(0.3)		
40	94	0.3(0.1)		
40	93	0.5(0.1)		
40	92	1.5(0.2)		
40	91	3.0(0.2)		
40	90	3.8(0.3)		
40	89	3.6(0.3)		

- [1] B. Blank, S. Andriamonje, R. Del Moral, J. P. Dufour, A. Fleury, T. Josso, M. S. Pravikoff, S. Czajkowski, Z. Janas, A. Piechaczek, E. Roeckl, K.-H. Schmidt, K. Sümmerer, W. Trinder, M. Weber, T. Brohm, A. Grewe, E. Hanelt, A. Heinz, A. Junghans, C. Röhl, S. Steinhäuser, B. Voss, and M. Pfützner, *Phys. Rev. C* **50**, 2398 (1994).
- [2] A. Stolz, T. Faestermann, J. Friese, P. Kienle, H.-J. Körner, M. Münch, R. Schneider, E. Wefers, K. Zeitelhack, K. Sümmerer, H. Geissel, J. Gerl, G. Münzenberg, C. Schlegel, R. S. Simon, H. Weick, M. Hellström, M. N. Mineva, and P. Thirolf, *Phys. Rev. C* **65**, 064603 (2002).
- [3] H. Suzuki, T. Kubo, N. Fukuda, N. Inabe, D. Kameda, H. Takeda, K. Yoshida, K. Kusaka, Y. Yanagisawa, M. Ohtake, H. Sato, Y. Shimizu, H. Baba, M. Kurokawa, T. Ohnishi, K. Tanaka, O. Tarasov, D. Bazin, D. Morrissey, B. Sherrill, K. Ieki, D. Murai, N. Iwasa, A. Chiba, Y. Ohkoda, E. Ideguchi, S. Go, R. Yokoyama, T. Fujii, D. Nishimura, H. Nishibata, S. Momota, M. Lewitowicz, G. DeFrance, I. Celikovic, and K. Steiger, *Nucl. Instrum. Methods Phys. Res. B* **317**, 756 (2013).
- [4] O. B. Tarasov, D. S. Ahn, D. Bazin, N. Fukuda, A. Gade, M. Hausmann, N. Inabe, S. Ishikawa, N. Iwasa, K. Kawata, T. Komatsubara, T. Kubo, K. Kusaka, D. J. Morrissey, M. Ohtake, H. Otsu, M. Portillo, T. Sakakibara, H. Sakurai, H. Sato, B. M. Sherrill, Y. Shimizu, A. Stolz, T. Sumikama, H. Suzuki, H. Takeda, M. Thoennessen, H. Ueno, Y. Yanagisawa, and K. Yoshida, *Phys. Rev. Lett.* **121**, 022501 (2018).
- [5] O. B. Tarasov, M. Portillo, D. J. Morrissey, A. M. Amthor, L. Bandura, T. Baumann, D. Bazin, J. S. Berryman, B. A. Brown, G. Chubarian, N. Fukuda, A. Gade, T. N. Ginter, M. Hausmann, N. Inabe, T. Kubo, J. Pereira, B. M. Sherrill, A. Stolz, C. Sumithrarachichi, M. Thoennessen, and D. Weissshaar, *Phys. Rev. C* **87**, 054612 (2013).
- [6] T. Baumann, A. M. Amthor, D. Bazin, B. A. Brown, C. M. Folden III, A. Gade, T. N. Ginter, M. Hausmann, M. Matoš, D. J. Morrissey, M. Portillo, A. Schiller, B. M. Sherrill, A. Stolz, O. Tarasov, and M. Thoennessen, *Nature (London)* **449**, 1022 (2007).
- [7] W. Wlazło, T. Enqvist, P. Armbruster, J. Benlliure, M. Bernas, A. Boudard, S. Czajkowski, R. Legrain, S. Leray, B. Mustapha, M. Pravikoff, F. Rejmund, K.-H. Schmidt, C. Stéphan, J. Taieb, L. Tassan-Got, and C. Volant, *Phys. Rev. Lett.* **84**, 5736 (2000).
- [8] C. Bowman, E. Arthur, P. Lisowski, G. Lawrence, R. Jensen, J. Anderson, B. Blind, M. Cappiello, J. Davidson, T. England, L. Engel, R. Haight, H. Hughes, J. Ireland, R. Krakowski, R. LaBauve, B. Letellier, R. Perry, G. Russell, K. Staudhammer, G. Versamis, and W. Wilson, *Nucl. Instrum. Methods Phys. Res. A* **320**, 336 (1992).
- [9] H. Wang, H. Otsu, H. Sakurai, D. Ahn, M. Aikawa, P. Doornenbal, N. Fukuda, T. Isobe, S. Kawakami, S. Koyama, T. Kubo, S. Kubono, G. Lorusso, Y. Maeda, A. Makinaga, S. Momiyama, K. Nakano, M. Niikura, Y. Shiga, P.-A. Söderström, H. Suzuki, H. Takeda, S. Takeuchi, R. Taniuchi, Y. Watanabe, Y. Watanabe, H. Yamasaki, and K. Yoshida, *Phys. Rev. Lett.* **754**, 104 (2016).
- [10] H. Wang, H. Otsu, H. Sakurai, D. Ahn, M. Aikawa, T. Ando, S. Araki, S. Chen, C. Nobuyuki, P. Doornenbal, N. Fukuda, T. Isobe, S. Kawakami, S. Kawase, T. Kin, Y. Kondo,

- S. Koyama, S. Kubono, Y. Maeda, A. Makinaga, M. Matsushita, T. Matsuzaki, S. Michimasa, S. Momiyama, S. Nagamine, T. Nakamura, K. Nakano, M. Niikura, T. Ozaki, A. Saito, T. Saito, Y. Shiga, M. Shikata, Y. Shimizu, S. Shimoura, T. Sumikama, P.-A. Söderström, H. Suzuki, H. Takeda, S. Takeuchi, R. Taniuchi, Y. Togano, J. Tsubota, M. Uesaka, Y. Watanabe, Y. Watanabe, K. Wimmer, T. Yamamoto, and K. Yoshida, *Progr. Theor. Exp. Phys.* **2017**, 021D01 (2017).
- [11] S. Kawase, K. Nakano, Y. Watanabe, H. Wang, H. Otsu, H. Sakurai, D. S. Ahn, M. Aikawa, T. Ando, S. Araki, S. Chen, N. Chiga, P. Doornenbal, N. Fukuda, T. Isobe, S. Kawakami, T. Kin, Y. Kondo, S. Koyama, S. Kubono, Y. Maeda, A. Makinaga, M. Matsushita, T. Matsuzaki, S. Michimasa, S. Momiyama, S. Nagamine, T. Nakamura, M. Niikura, T. Ozaki, A. Saito, T. Saito, Y. Shiga, M. Shikata, Y. Shimizu, S. Shimoura, T. Sumikama, P.-A. Söderström, H. Suzuki, H. Takeda, S. Takeuchi, R. Taniuchi, Y. Togano, J. Tsubota, M. Uesaka, Y. Watanabe, K. Wimmer, T. Yamamoto, and K. Yoshida, *Progr. Theor. Exp. Phys.* **2017**, 093D03 (2017).
- [12] C. Villagrasa-Canton, A. Boudard, J.-E. Ducret, B. Fernandez, S. Leray, C. Volant, P. Armbruster, T. Enqvist, F. Hammache, K. Helariutta, B. Jurado, M.-V. Ricciardi, K.-H. Schmidt, K. Sümmerer, F. Vivès, O. Yordanov, L. Audouin, C.-O. Bacri, L. Ferrant, P. Napolitani, F. Rejmund, C. Stéphan, L. Tassan-Got, J. Benlliure, E. Casarejos, M. Fernandez-Ordóñez, J. Pereira, S. Czajkowski, D. Karamanis, M. Pravikoff, J. S. George, R. A. Mewaldt, N. Yanasak, M. Wiedenbeck, J. J. Connell, T. Faestermann, A. Heinz, and A. Junghans, *Phys. Rev. C* **75**, 044603 (2007).
- [13] F. Rejmund, B. Mustapha, P. Armbruster, J. Benlliure, M. Bernas, A. Boudard, J. Dufour, T. Enqvist, R. Legrain, S. Leray, K.-H. Schmidt, C. Stéphan, J. Taieb, L. Tassan-Got, and C. Volant, *Nucl. Phys. A* **683**, 540 (2001).
- [14] J. Benlliure, M. Fernández-Ordóñez, L. Audouin, A. Boudard, E. Casarejos, J. E. Ducret, T. Enqvist, A. Heinz, D. Henzlova, V. Henzl, A. Kelić, S. Leray, P. Napolitani, J. Pereira, F. Rejmund, M. V. Ricciardi, K.-H. Schmidt, C. Schmitt, C. Stéphan, L. Tassan-Got, C. Volant, C. Villagrasa, and O. Yordanov, *Phys. Rev. C* **78**, 054605 (2008).
- [15] P. Napolitani, K.-H. Schmidt, L. Tassan-Got, P. Armbruster, T. Enqvist, A. Heinz, V. Henzl, D. Henzlova, A. Kelić, R. Pleskač, M. V. Ricciardi, C. Schmitt, O. Yordanov, L. Audouin, M. Bernas, A. Lafriaskh, F. Rejmund, C. Stéphan, J. Benlliure, E. Casarejos, M. Fernandez Ordóñez, J. Pereira, A. Boudard, B. Fernandez, S. Leray, C. Villagrasa, and C. Volant, *Phys. Rev. C* **76**, 064609 (2007).
- [16] J. Alcántara-Núñez, J. Benlliure, C. Paradela, C. Pérez-Loureiro, J. L. Rodríguez-Sánchez, L. Audouin, A. Boudard, E. Casarejos, T. Enqvist, F. Farget, M. Fernández-Ordóñez, A. Heinz, V. Henzl, D. Henzlova, A. Kelić-Heil, A. Lafriaskh, S. Leray, P. Napolitani, J. Pereira, M. V. Ricciardi, C. Stéphan, K.-H. Schmidt, C. Schmitt, L. Tassan-Got, C. Villagrasa, C. Volant, and O. Yordanov, *Phys. Rev. C* **92**, 024607 (2015).
- [17] L. Giot, J. Alcántara-Núñez, J. Benlliure, D. Pérez-Loureiro, L. Audouin, A. Boudard, E. Casarejos, T. Enqvist, J. Ducret, B. Fernández-Domínguez, M. F. Ordóñez, F. Farget, A. Heinz, V. Henzl, D. Henzlova, A. Kelić-Heil, A. Lafriaskh, S. Leray, P. Napolitani, C. Paradela, J. Pereira, M. Ricciardi, C. Stéphan, K.-H. Schmidt, C. Schmitt, L. Tassan-Got, C. Villagrasa, C. Volant, and O. Yordanov, *Nucl. Phys. A* **899**, 116 (2013).
- [18] C. Paradela, L. Tassan-Got, J. Benlliure, J. L. Rodríguez-Sánchez, L. Audouin, A. Boudard, E. Casarejos, T. Enqvist, J. E. Ducret, F. Farget, B. Fernández-Domínguez, M. Fernández Ordóñez, L. Giot, A. Heinz, V. Henzl, D. Henzlova, A. Kelić-Heil, A. Lafriaskh, S. Leray, P. Napolitani, J. Pereira, D. Pérez-Loureiro, M. V. Ricciardi, C. Stéphan, K.-H. Schmidt, C. Schmitt, C. Villagrasa, C. Volant, and O. Yordanov, *Phys. Rev. C* **95**, 044606 (2017).
- [19] D. Henzlova, K.-H. Schmidt, M. V. Ricciardi, A. Kelić, V. Henzl, P. Napolitani, L. Audouin, J. Benlliure, A. Boudard, E. Casarejos, J. E. Ducret, T. Enqvist, A. Heinz, A. Junghans, B. Jurado, A. Krása, T. Kurtukian, S. Leray, M. F. Ordóñez, J. Pereira, R. Pleskač, F. Rejmund, C. Schmitt, C. Stéphan, L. Tassan-Got, C. Villagrasa, C. Volant, A. Wagner, and O. Yordanov, *Phys. Rev. C* **78**, 044616 (2008).
- [20] U. Singh, D. Filges, F. Goldenbaum, B. Kamys, Z. Rudy, and S. K. Sharma, *Eur. Phys. J. A* **54**, 109 (2018).
- [21] T. Kubo, D. Kameda, H. Suzuki, N. Fukuda, H. Takeda, Y. Yanagisawa, M. Ohtake, K. Kusaka, K. Yoshida, N. Inabe, T. Ohnishi, A. Yoshida, K. Tanaka, and Y. Mizoi, *Progr. Theor. Exp. Phys.* **2012**, 03C003 (2012).
- [22] N. Fukuda, T. Kubo, T. Ohnishi, N. Inabe, H. Takeda, D. Kameda, and H. Suzuki, *Nucl. Instrum. Methods Phys. Res. B* **317**, 323 (2013).
- [23] Y. Maeda, H. Sakai, K. Hatanaka, and A. Tamii, *Nucl. Instrum. Methods Phys. Res. A* **490**, 518 (2002).
- [24] C. Scheidenberger, T. Stöhlker, W. Meyerhof, H. Geissel, P. Mokler, and B. Blank, *Nucl. Instrum. Methods Phys. Res. B* **142**, 441 (1998).
- [25] O. B. Tarasov and D. Bazin, *Nucl. Instrum. Methods Phys. Res. B* **266**, 4657 (2008).
- [26] K. Sümmerer and B. Blank, *Phys. Rev. C* **61**, 034607 (2000).
- [27] T. Sato, K. Niita, N. Matsuda, S. Hashimoto, Y. Iwamoto, S. Noda, T. Ogawa, H. Iwase, H. Nakashima, T. Fukahori, K. Okumura, T. Kai, S. Chiba, T. Furuta, and L. Sihver, *J. Nucl. Sci. Technol.* **50**, 913 (2013).
- [28] A. Kelić, K.-H. Schmidt, T. Enqvist, A. Boudard, P. Armbruster, J. Benlliure, M. Bernas, S. Czajkowski, R. Legrain, S. Leray, B. Mustapha, M. Pravikoff, F. Rejmund, C. Stéphan, J. Taïeb, L. Tassan-Got, C. Volant, and W. Wlazło, *Phys. Rev. C* **70**, 064608 (2004).
- [29] K.-H. Schmidt, T. Brohm, H.-G. Clerc, M. Dornik, M. Fauerbach, H. Geissel, A. Grewe, E. Hanelt, A. Junghans, A. Magel, W. Morawek, G. Münzenberg, F. Nickel, M. Pfützner, C. Scheidenberger, K. Sümmerer, D. Vieira, B. Voss, and C. Ziegler, *Phys. Lett. B* **300**, 313 (1993).
- [30] P. Napolitani, K.-H. Schmidt, A. S. Botvina, F. Rejmund, L. Tassan-Got, and C. Villagrasa, *Phys. Rev. C* **70**, 054607 (2004).
- [31] C. Schmitt, K.-H. Schmidt, and A. Kelić-Heil, *Phys. Rev. C* **90**, 064605 (2014).
- [32] B. T. Roeder, K. W. Kemper, N. Aoi, D. Bazin, M. Bowen, C. M. Campbell, J. M. Cook, D.-C. Dinca, A. Gade, T. Glasmacher, H. Iwasaki, S. Kanno, T. Motobayashi, W. F. Mueller, T. Nakamura, H. Sakurai, H. Suzuki, S. Takeuchi, J. R. Terry, K. Yoneda, and H. Zwahlen, *Phys. Rev. C* **74**, 034602 (2006).
- [33] K. Niita, S. Chiba, T. Maruyama, T. Maruyama, H. Takada, T. Fukahori, Y. Nakahara, and A. Iwamoto, *Phys. Rev. C* **52**, 2620 (1995).

- [34] T. Ogawa, T. Sato, S. Hashimoto, D. Satoh, S. Tsuda, and K. Niita, *Phys. Rev. C* **92**, 024614 (2015).
- [35] S. Furihata, *Nucl. Instrum. Methods Phys. Res. B* **171**, 251 (2000).
- [36] T. Ogawa, M. Morev, T. Sato, and S. Hashimoto, *Nucl. Instrum. Methods Phys. Res. B* **300**, 35 (2013).
- [37] S. Chiba, K. Niita, and O. Iwamoto, *Phys. Rev. C* **54**, 3302 (1996).
- [38] M. Mocko, M. B. Tsang, Z. Y. Sun, N. Aoi, J. M. Cook, F. Delaunay, M. A. Famiano, H. Hui, N. Imai, H. Iwasaki, W. G. Lynch, T. Motobayashi, M. Niikura, T. Onishi, A. M. Rogers, H. Sakurai, A. Stolz, H. Suzuki, E. Takeshita, S. Takeuchi, and M. S. Wallace, *Phys. Rev. C* **76**, 014609 (2007).
- [39] M. Mocko, M. B. Tsang, L. Andronenko, M. Andronenko, F. Delaunay, M. Famiano, T. Ginter, V. Henzl, D. Henzlová, H. Hua, S. Lukyanov, W. G. Lynch, A. M. Rogers, M. Steiner, A. Stolz, O. Tarasov, M.-J. van Goethem, G. Verde, W. S. Wallace, and A. Zalessov, *Phys. Rev. C* **74**, 054612 (2006).
- [40] S. Nakayama, N. Furutachi, O. Iwamoto, and Y. Watanabe, *Phys. Rev. C* **98**, 044606 (2018).
- [41] A. Boudard, J. Cugnon, J.-C. David, S. Leray, and D. Mancusi, *Phys. Rev. C* **87**, 014606 (2013).
- [42] D. Mancusi, A. Boudard, J. Carbonell, J. Cugnon, J.-C. David, and S. Leray, *Phys. Rev. C* **91**, 034602 (2015).
- [43] M. Ricciardi, A. Ignatyuk, A. Kelić, P. Napolitani, F. Rejmund, K.-H. Schmidt, and O. Yordanov, *Nucl. Phys. A* **733**, 299 (2004).
- [44] I.-M. Ladenbauer and L. Winsberg, *Phys. Rev.* **119**, 1368 (1960).
- [45] M. Dikšić and L. Yaffe, *J. Inorg. Nucl. Chem.* **39**, 1299 (1977).
- [46] S. B. Kaufman and E. P. Steinberg, *Phys. Rev. C* **22**, 167 (1980).